Electron-impact ionization of N_2 at large momentum transfer above the double-ionization threshold

D. B. Jones,* M. Yamazaki, N. Watanabe, and M. Takahashi†
Institute of Multidisciplinary Research for Advanced Materials, Tohoku University, Sendai 980-8577, Japan
(Received 15 October 2012; published 18 December 2012)

High-energy electron-impact $(e,2e)$ measurements under large momentum-transfer kinematics for molecular nitrogen are reported over an extended binding-energy range. These measurements are supplemented with symmetry-adapted cluster configuration-interaction calculations to provide insight into the behavior of ionization mechanisms above the double-ionization threshold. Here, it was found that ionization-excitation processes make a significant partial contribution to the ionization phenomena for binding energies above the lowest double-ionization potential.

DOI: 10.1103/PhysRevA.86.062707 PACS number(s): 34.80.Gs

I. INTRODUCTION

Binary $(e,2e)$ at large momentum transfer or electron momentum spectroscopy (EMS) has become a powerful tool for gaining significant insight into the electronic structure of matter as it can probe the momentum dependence of an energy-selected ionization process [1–6]. The evolution of this technique has enabled it to become an important quantitative test for quantum chemical models through the application of the plane-wave impulse approximation (PWIA). However, this form of spectroscopy has historically been limited by the long experimental run times that are required to measure the weak scattering process that simulates a collision between two free electrons. The improved collection efficiency of multichannel spectrometers, where the momentum dependence of a range of energy-selected ionization processes can be obtained simultaneously, has enabled this technique to be applied to molecular-frame $(e,2e+M)$ experiments on H_2 [7,8]. This technique has recently been extended to consider $(e,2e+M)$ experiments on N_2 for binding energies up to 80 eV where the two outgoing electrons and a dissociation fragment ion are detected in triple coincidence [9]. In order to fully evaluate those triple coincident results, a detailed understanding of the electron-impact ionization of the states at energies lying above the lowest double-ionization threshold (43 eV [10]) is required. Gaining such an understanding is nontrivial as ionization mechanisms relating to double ionization become available and may combine with the contribution from single-ionization processes.

Although significant progress has been made at understanding the collision mechanisms for electron-impact ionization at binding energies above the double-ionization onset under kinematical conditions where there is a low momentum transfer and the outgoing electron energies are small [11], it is only recently that high-energy electron-impact ionization experiments at a large momentum transfer over extended binding-energy ranges for atomic targets have been extended to the water molecule [12]. The extension of this technique is particularly important for determining if spectroscopic sum rules [1,2] can be reasonably applied to molecular targets. Such experiments are also essential for determining the influence of the projectile on the ionization process. Indeed, electron-impact ionization processes have exhibited significantly enhanced cross sections over photoionization through contributions from giant resonances [13]. Lastly, such experiments may provide key insight into the relationship between single ionization, autoionization, and direct double-ionization mechanisms. It is, therefore, particularly important to characterize and to understand the nature of electron-impact ionization processes under high-impact energy and large momentum-transfer kinematics for states lying above the lowest double-ionization potential.

The spectroscopy of N_2 has attracted significant interest, both experimentally and theoretically, over an extended period of time. Indeed, the combination of photoelectron spectroscopy (PES) [14,15] and EMS [16,17] experiments with sophisticated calculations, such as those based on the Green's function [16] or configuration-interaction (CI) methods [14,18,19], has provided an excellent account of the photon- and electron-impact ionizations of the outer- and inner-valence regions up to the first double-ionization threshold. At higher binding energies, a number of singly and doubly ionized states have been identified through resonant Auger or de-excitation spectroscopy [20] and Auger spectroscopy [20,21]. These techniques have provided sensitive information regarding the relaxation of the target to fill the core-hole state. To our knowledge, however, it is only the previous x-ray photoelectron spectroscopy (XPS) paper [22] that has considered the valence ionization of N_2 to produce states lying above the double-ionization threshold.

In order to further elucidate the origins of ionization mechanisms of high binding-energy states, we have performed an $(e,2e)$ experiment for N_2 over an extended binding-energy range, that includes binding energies above the lowest double-ionization threshold. This experiment significantly extends the binding-energy range examined in previous EMS papers on N_2 [16,17]. In order to interpret these results, the experiments have been supplemented with a limited symmetry-adapted cluster configuration-interaction (SAC-CI) calculation that describes the singly ionized states found at higher binding energies.

II. METHOD

The binary $(e,2e)$ or electron momentum spectroscopy technique considers the electron-impact ionization of the target

*Present address: School of Chemical and Physics Sciences, Flinders University, GPO Box 2100, Adelaide, South Australia 5001, Australia.
†Corresponding author: masahiko@tagen.tohoku.ac.jp

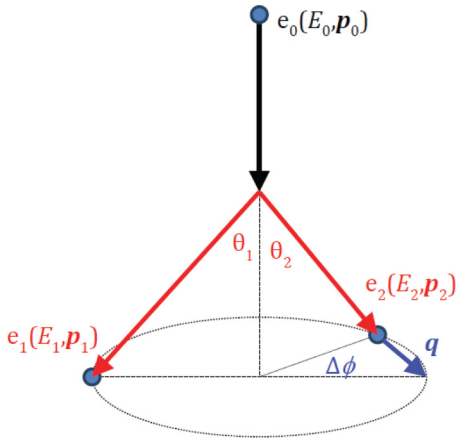

FIG. 1. (Color online) Schematic of the symmetric noncoplanar $(e,2e)$ experiment at large momentum transfer.

where the energies and momenta of both the scattered and the ejected electrons are determined in coincidence. This reaction is schematically shown in Fig. 1. The conservation of energy and linear momentum require

$$\mathrm{IP} = E_0 - E_1 - E_2, \tag{1}$$

and

$$\boldsymbol{q} = \boldsymbol{p}_0 - \boldsymbol{p}_1 - \boldsymbol{p}_2. \tag{2}$$

Here, E_i and $\boldsymbol{p}_i$ $(i = 0-2)$ are the energy and momenta of the incident and scattered electrons, respectively. IP is the ionization potential, and $\boldsymbol{q}$ is the momentum of the recoiling ion. The ability of this technique to provide structure information relies on the kinematics being chosen in such a way that all of the momentum transferred during the collision is absorbed by the ejected electron. If all of the momentum is transferred to the ejected electron, the recoil momentum of the ion is equal in magnitude and is opposite in sign to the momentum of the bound electron at the instance of ionization $\boldsymbol{p}$ such that

$$\boldsymbol{p} = -\boldsymbol{q}. \tag{3}$$

The present experiment is conducted in the symmetric noncoplanar geometry where two electrons are detected with equal energies $(E_1 = E_2)$ while making the same polar angles with respect to the incident-beam direction $(\theta_1 = \theta_2 = 45^\circ)$. When the incident electron energy E_0 is fixed, varying the detection energy of the outgoing electrons enables the binding energy $(E = E_0 - E_1 - E_2)$ to be scanned. Furthermore, when the electron energies and polar angles are fixed, the recoil momentum magnitude is solely a function of the azimuthal angle difference $\Delta\phi$,

$$q = \sqrt{(p_0 - \sqrt{2}p_1)^2 + \left[\sqrt{2}p_1 \sin\left(\frac{\Delta\phi}{2}\right)\right]^2}. \tag{4}$$

The experiment has been conducted using our specifically designed molecular frame $(e,2e)$ spectrometer, which has previously been described in detail [7]. The present experiment was conducted in parallel with new triple coincident experiments for N_2, and those results were presented elsewhere [9]. Both of these experiments were performed using an incident electron-beam energy of $E_0 = 1230$ eV. Here, large apertures of 2 and 5 mm were used in the spectrometer to maximize the true triple coincidence signal and weak signals from states with very high binding energies. Although this degrades the energy $(\Delta E \sim 8$ eV) and momentum resolution $(\Delta q \sim 0.3$ a.u. at $q = 1.0$ a.u.) of the $(e,2e)$ experiment, they are required to facilitate a direct comparison between the $(e,2e)$ and $(e,2e+M)$ results.

For the full details of the binary $(e,2e)$ reaction, the reader is referred to a number of excellent review articles [1–6]. Briefly though, the $(e,2e)$ scattering process with high incident and outgoing particle energies and involving a large momentum transfer to the ejected electron has been well described through the PWIA. The cross section in this regime is given by

$$\sigma_{if}(p) = (2\pi)^4 \frac{p_1 p_2}{p_0} f_{ee} \sum_{av} \left|\left\langle \boldsymbol{p}\Psi_f^{N-1} \mid \Psi_i^N \right\rangle\right|^2. \tag{5}$$

Here, f_{ee} is the factor describing the strength of a collision between two free electrons [4,23]. The structure factor $|\langle \boldsymbol{p}\Psi_f^{N-1}|\Psi_i^N\rangle|^2$ is the square of the momentum space representation of the quasiparticle or Dyson orbital. This Dyson orbital describes the one-hole overlap between the initial N-electron neutral (Ψ_i^N) and final $(N-1)$-electron wave functions (Ψ_f^{N-1}) as a function of the momentum of the electron when it is ionized $(\boldsymbol{p})$. Although Dyson orbitals can be fully evaluated in a configuration-interaction picture, they can often be well described in a weak-coupling approximation [2,4] by the ionized Hartree-Fock (HF) or Kohn-Sham (KS) orbital [24],

$$\left\langle \boldsymbol{p}\Psi_f^{N-1} \mid \Psi_i^N \right\rangle = \sqrt{S_a^f}\,\phi_a(\boldsymbol{p}). \tag{6}$$

Here, S_a^f is the associated spectroscopic strength of the transition. Note that the sum of the spectroscopic factors belonging to a transition manifold is unity. These so-called target HF [1,4] or KS approximations [25–27] are valid only when the respective HF or KS target wave function produces a good description of the initial target state.

To evaluate the spectroscopic behavior at binding energies above the double-ionization potential, we have performed SAC-CI calculations with the general-R method [28] for states with binding energies up to 65 eV. The SAC-CI general-R method describes multielectron processes with high accuracy owing to the inclusion of higher-excitation operators while being computationally more efficient than conventional or multireference configuration-interaction methods [29]. Indeed, the SAC-CI method has been previously used to describe the high binding-energy behavior of water [12] and CO_2 [30] above their lowest double-ionization potentials. In order for the calculations of deep-inner valence states to become tractable, we have restricted the included excitation operators to triples. In these calculations, a double-ζ-polarized basis set [31] with additional Rydberg s and p functions [32] has been employed. Although this basis set is quite small, it is also required to extend the calculations over this large energy range.

In order to directly compare the theoretical and experimental data, we generate synthetic angle-resolved binding-energy spectra. These spectra are obtained by first generating a synthetic SAC-CI binding-energy spectrum for each one-hole configuration $I_a(E)$. Here, the spectroscopic factors, taken as the square of the one-hole coefficients derived in the

SAC-CI calculations, are convolved with the present energy resolution of 8 eV. Note that, in the present calculation, configuration-interaction coefficients were only recovered for configurations with $|c| > 0.03$. These one-hole spectra are then converted into momentum-weighted spectra $I_a^{AR}(E,\Delta\phi)$ by multiplying the one-hole synthetic binding-energy spectra by the theoretical PWIA EMS cross section for the ionized orbital evaluated at the recoil momentum value associated with the azimuthal angle difference and outgoing electron energies, $\sigma_a(E,q(\Delta\phi))$,

$$I_a^{AR}(E,\Delta\phi) = I_a(E)\sigma_a(E,q(\Delta\phi)). \quad (7)$$

Here, the EMS cross sections are derived from orbital momentum densities that have been obtained within the target Kohn-Sham approximation [25–27] using the Becke three-parameter Lee, Yang, and Parr density functional employed with an augmented correlation-consistent polarized valence triple-ζ basis set (B3LYP/aug-cc-pVTZ) [33–36]. These orbital momentum density calculations were performed using the HEMS program [37]. Note that these theoretical EMS cross sections have been convoluted with the present experimental energy and angular resolutions following a similar procedure to that outlined by Migdall *et al.* [38]. Finally, the momentum-weighted one-hole spectra are then summed over the one-hole states to give the final synthetic angle-resolved binding-energy spectra. By producing the synthetic spectra in this way, it can be directly compared with the experimental angle-resolved binding-energy spectra. This is advantageous in the present paper as it removes any ambiguity in the spectral assignment of closely lying unresolved features owing to the limited experimental energy and momentum resolutions. Note that the present structure calculations have been performed in the GAUSSIAN 98/03 suites of packages [39,40].

III. RESULTS AND DISCUSSION

In Fig. 2, we present representative $(e,2e)$ binding-energy spectra at azimuthal angle differences ($\Delta\phi$'s) of 0°, 8°, and 16°. These experimental data are also directly compared with the synthetic angle-resolved binding-energy spectra in the same figure. Here, the experimental data have been globally renormalized to the outer-valence region ($E <$ 25 eV) of the synthetic $\Delta\phi = 0°$ angle-resolved spectrum. To assist readers in observing the behavior at high binding energies, we also include the experimental and synthetic spectra after being scaled by a factor of 10 for binding energies greater than 45 eV. By studying the spectral intensity at multiple azimuthal angle differences, we can evaluate the momentum dependence of the individual ionization channels. In each binding-energy spectrum, we observe three distinct features that correspond to the outer-valence ($E < 25$ eV), inner-valence ($25 \leqslant E < 45$ eV), and deep inner-valence ($E \geqslant 45$ eV) regions. The reader is referred to any of the earlier papers [14–19,22] for detailed discussions of the outer- and inner-valence behaviors. Briefly, the present experimental resolution limits the ability to resolve the individual ionization features. This limitation leads to a significant overlap of the ionization bands possessing different orbital characters that somewhat mask the momentum dependence of each individual ionization channel. Note that the compromised

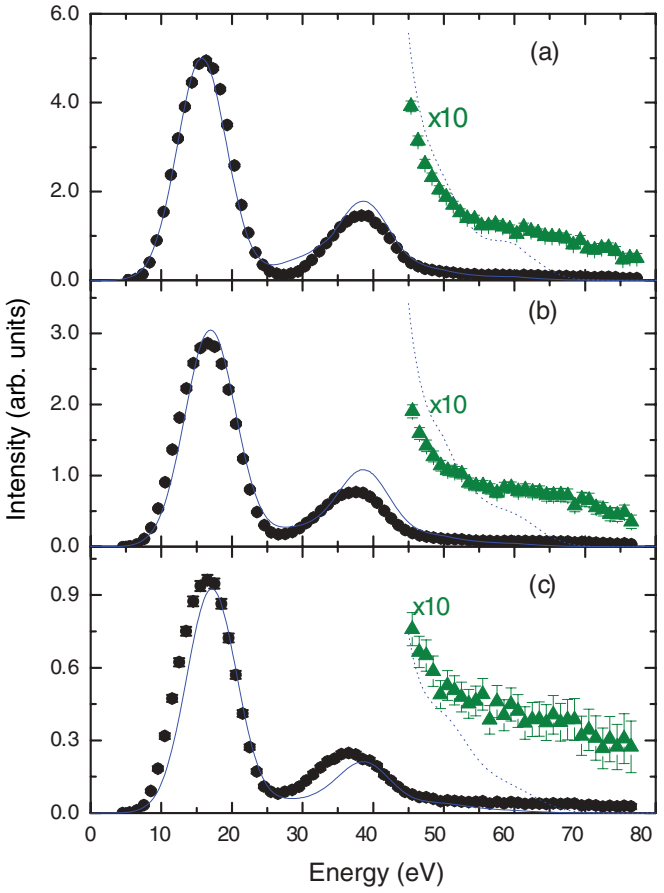

FIG. 2. (Color online) (•): The measured $(e,2e)$ binding-energy spectra of N_2 at (a) $\Delta\phi = 0°$, (b) $\Delta\phi = 8°$, and (c) $\Delta\phi = 16°$. Also presented is (———-): the synthetic binding-energy spectra. At energies above 45 eV, (▲): the present experimental data and (– –): theoretical spectra have been multiplied by a factor of 10. See the text for further details.

energy resolution is an essential requirement to observe the weak intensity of the spectra at high binding energies. Despite this, by generating synthetic angle-resolved binding energy spectra, we can directly assess the momentum dependence of the individual ionization channels. Here, the synthetic binding-energy spectra provide a reasonable description of the outer- and inner-valence-state behaviors at all of the azimuthal angles considered given the limitations employed in the calculations. This fair agreement suggests confidence in the calculation for describing the behavior at higher binding energies.

In order to offer qualitative information on the momentum dependence of each ionization channel, in Fig. 3, we present the experimental and theoretical binding-energy spectra at azimuthal angle differences of 0°, 8°, and 16°, again, with each spectrum being normalized to the maximum spectral intensity in the inner-valence region. In this inner-valence ionization region, the spectral intensity is dominated by the shake-up satellites of the $(2\sigma_g)^{-1}$ manifold [14–19]. The spectral intensity observed for this inner-valence transition is, therefore, predominantly "s-like" in character; having a maximum spectral intensity at $p \sim 0$ ($\Delta\phi = 0$) that decreases as the magnitude of the recoil momentum increases [16,19]. Note that all of the shake-up states that belong to the $(2\sigma_g)^{-1}$ manifold

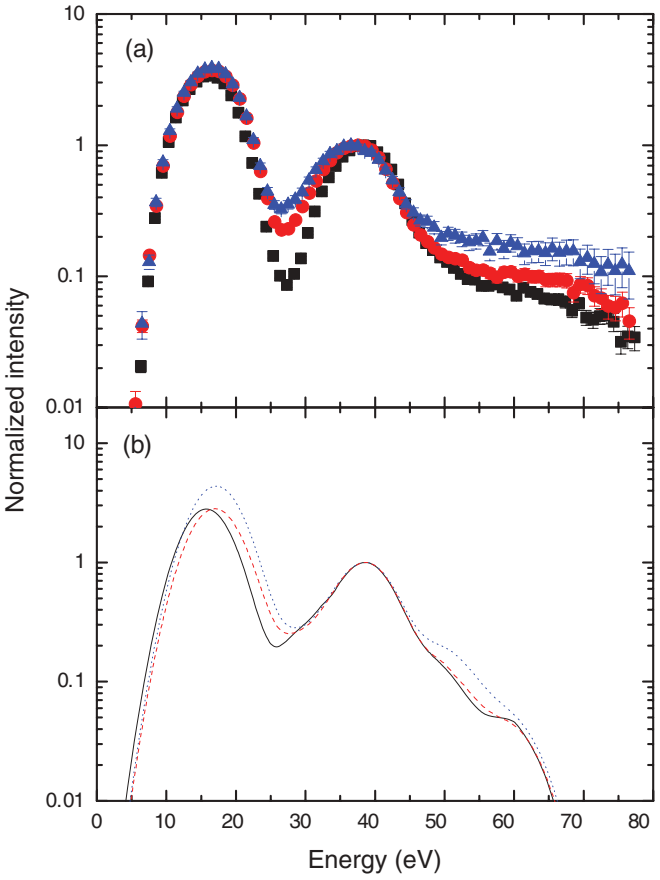

FIG. 3. (Color online) The normalized $(e,2e)$ binding-energy spectra of N_2. (a) Experimental data for (■): $\Delta\phi = 0^\circ$; (●): $\Delta\phi = 8^\circ$; and (▲): $\Delta\phi = 16^\circ$. (b) Synthetic spectra for (—-): $\Delta\phi = 0^\circ$; (– –): $\Delta\phi = 8^\circ$; and (· · · ·): $\Delta\phi = 16^\circ$. See the text for further details.

exhibit the same momentum dependence with their differences in magnitude reflecting their respective spectroscopic strengths [see Eq. (6)]. The normalization procedure employed to produce Fig. 3, therefore, fixes the contribution from states belonging to the $(2\sigma_g)^{-1}$ manifold at all binding energies. Variations in behavior as the azimuthal angle changes, within the target HF or KS approximation, indicate the presence of states possessing different momentum dependences. In the case of N_2, the differences in momentum dependence reflect different final-state symmetries. In particular, the spectral intensities of the $^2\Sigma_u$ or $^2\Pi_u$ manifolds are expected to be at their lowest at $p \sim 0$ ($\Delta\phi = 0^\circ$) due to their characteristic nonzero angular momentum contributions [16,19]. As such, the binding-energy spectra at $p \sim 0$ ($\Delta\phi = 0^\circ$) are expected to indicate the strength of the $^2\Sigma_g$ manifold contribution. Deviations from the $\Delta\phi = 0^\circ$ binding-energy spectrum as the azimuthal angle varies in the normalized figure are then expected to clearly identify contributions from either the $^2\Sigma_u$ or the $^2\Pi_u$ manifolds.

The spectroscopic behavior for the high-lying states found at binding energies above 40 eV is now discussed in detail with reference to both the angle-resolved binding-energy spectra (Fig. 2) and the intensity-normalized spectra (Fig. 3). The first observation from Fig. 2 is that the spectral intensity is broadly distributed and decreasing as the binding energy increases. This behavior is consistent for binding-energy spectra measured at all azimuthal angle differences. We also note that the maximum spectral intensity occurs at $\Delta\phi = 0^\circ$ for all binding energies. Within the one-particle picture, such contributions characteristically reflect an important s-like contribution from states belonging to the $^2\Sigma_g$ manifold. The persistence of this behavior over the entire binding energy range above 40 eV, with no noticeable features, suggests that a number of weak satellites are distributed over the entire energy range. These experimental observations are consistent with the behavior found in the synthetic spectra. Specifically, 20 $^2\Sigma_g$ satellite states are recovered with nonzero monopole intensities in the 40–50-eV binding-energy range having a combined monopole intensity of 0.069. This situation is much more dramatic at binding energies above 50 eV where 57 $^2\Sigma_g$ satellite states are recovered with nonzero monopole intensities with a summed monopole intensity of 0.055. Note that, of these 57 $^2\Sigma_g$ satellite states, 45 were recovered with monopole intensities less than 0.001. Thus, most of these states are not contributing to the synthetic spectra derived using the square of the one-hole coefficients. As the combined monopole intensity of these states is 0.012, their contributions may go some way to explain the observed differences between the synthetic and the experimental spectra at higher binding energies.

The normalized spectra in Fig. 3 provide further insight into the behavior of the spectra at high binding energies. For energies above ∼45 eV, we start to see significant variations between the binding-energy spectra measured at each azimuthal angle difference. Here, the normalized intensity increases as the azimuthal angle difference increases. This suggests that states from either or both of the $^2\Sigma_u$ or $^2\Pi_u$ manifolds, characterized by higher orbital angular momentum contributions, are also playing an important role in this binding-energy region. Note that this behavior is similar to that observed in the vicinity of ∼25 eV where a prominent $^2\Sigma_u$ satellite has been found in previous papers [16,18,19]. Also note that despite the presence of $^2\Sigma_u$ or $^2\Pi_u$ states, the band for ionization of the outer-valence orbitals only shows a slight variation with the change of azimuthal angle as the cross section is heavily weighted by contributions from the $^2\Sigma_g$ $(3\sigma_g)^{-1}$ state [16].

In order to offer more quantitative insight into the observed behavior, we now discuss the theoretical SAC-CI results in more detail. To assist in this discussion, a theoretical SAC-CI binding-energy spectrum, which details the respective contributions from states of different symmetries, is also presented in Fig. 4. Here, the spectrum is obtained by convolving each spectral feature with the experimental energy resolution and weighting that contribution by the monopole intensity of the transition and the states' degeneracy. We also present the ionization energies for states lying above 40 eV in Table I. As noted earlier, the SAC-CI result provides an excellent description of the outer- and inner-valence binding-energy regions despite the limitations employed in the present calculation. Indeed, the calculated ionization energies and monopole intensities in the outer- and inner-valence regions were found to be in good accord with more sophisticated SAC-CI calculations [18,19] and the previous higher-resolution EMS [16,17], XPS [22], or PES papers [14,15]. Although the small basis set and restricted operators affected the location

TABLE I. The present SAC-CI calculated ionization potentials (IPs) and pole strengths (PSs) for ionization potentials above 40 eV. Only those states with PSs that are greater than 0.002 are reported. The main configurations ($|c| > 0.3$) are also included. These values are compared with the previous XPS results [21]. See the text for further details.

XPS	Present SAC-CI			
IP (eV)	State	IP (eV)	PS	Main configurations
40.8	$^2\Pi_u$	40.90	0.006	$0.45(1\pi_u^{-2}2\pi_u) + 0.37(1\pi_u^{-2}2\pi_u)$
42.5	$^2\Sigma_g^+$	42.43	0.006	$0.35(1\pi_u^{-2}4\sigma_g) - 0.34(2\sigma_u^{-2}4\sigma_g) + 0.33(1\pi_u^{-2}5\sigma_g)$
	$^2\Sigma_u^+$	42.61	0.003	
	$^2\Sigma_g^+$	42.75	0.003	$0.62(3\sigma_g^{-2}6\sigma_g)$
	$^2\Sigma_u^+$	42.79	0.009	$0.46(1\pi_u^{-1}2\pi_u2\sigma_u^{-1}) + 0.40(3\sigma_g^{-1}4\sigma_g2\sigma_u^{-1}) - 0.39(2\sigma_u^{-1}5\sigma_g3\sigma_g^{-1})$ $- 0.38(3\sigma_g^{-1}5\sigma_g2\sigma_u^{-1}) + 0.35(2\sigma_u^{-1}4\sigma_g3\sigma_g^{-1})$
	$^2\Sigma_u^+$	43.00	0.007	$0.53(3\sigma_g^{-2}5\sigma_u) + 0.37(1\pi_u^{-1}2\pi_u2\sigma_u^{-1}) + 0.33(3\sigma_g^{-2}4\sigma_u)$ $+ 0.32(2\sigma_u^{-1}2\pi_u1\pi_u^{-1})$
44.0	$^2\Sigma_g^+$	43.81	0.007	$0.37(3\sigma_g^{-1}3\pi_u1\pi_u^{-1}) - 0.37(3\sigma_g^{-2}6\sigma_g) + 0.36(3\sigma_g^{-1}4\sigma_u2\sigma_u^{-1})$
	$^2\Sigma_u^+$	43.41	0.008	$0.51(2\sigma_u^{-1}5\sigma_g3\sigma_g^{-1}) - 0.46(3\sigma_g^{-1}4\sigma_g2\sigma_u^{-1}) - 0.46(2\sigma_u^{-1}4\sigma_g3\sigma_g^{-1})$ $+ 0.45(3\sigma_g^{-1}5\sigma_g2\sigma_u^{-1})$
	$^2\Sigma_g^+$	44.46	0.006	$0.51(3\sigma_g^{-1}3\pi_u1\pi_u^{-1}) - 0.33(3\sigma_g^{-1}4\sigma_u2\sigma_u^{-1}) - 0.36(2\sigma_u^{-1}4\sigma_u3\sigma_g^{-1})$
	$^2\Sigma_g^+$	45.96	0.005	$0.42(2\sigma_u^{-2}5\sigma_g) + 0.39(2\sigma_u^{-1}4\sigma_u3\sigma_g^{-1}) - 0.34(3\sigma_g^{-1}5\sigma_u2\sigma_u^{-1})$ $-0.31(3\sigma_g^{-1}3\sigma_u2\sigma_u^{-1})$
46.3	$^2\Sigma_g^+$	47.21	0.004	$0.55(1\pi_u^{-2}6\sigma_g) - 0.30(2\sigma_u^{-2}6\sigma_g)$
	$^2\Sigma_g^+$	47.70	0.015	$0.13(2\sigma_g^{-1}) + 0.47(1\pi_u^{-1}3\pi_u3\sigma_g^{-1})$
48.1	$^2\Sigma_g^+$	48.19	0.014	$0.11(2\sigma_g^{-1}) - 0.37(1\pi_u^{-1}3\pi_u3\sigma_g^{-1})$
	$^2\Pi_u$	48.40	0.008	$0.44(1\pi_u^{-2}3\pi_u) + 0.33(2\sigma_g^{-1}2\pi_g2\sigma_u^{-1})$
	$^2\Sigma_g^+$	48.63	0.003	$0.68(3\sigma_g^{-1}3\sigma_u2\sigma_u^{-1}) + 0.68(2\sigma_u^{-1}3\sigma_u3\sigma_g^{-1}) + 0.40(2\sigma_u^{-1}4\sigma_u3\sigma_g^{-1})$ $+ 0.39(3\sigma_g^{-1}4\sigma_u2\sigma_u^{-1}) - 0.35(2\sigma_u^{-1}5\sigma_u3\sigma_g^{-1})$
	$^2\Pi_u$	48.86	0.003	$0.51(1\pi_u^{-1}5\sigma_u2\sigma_u^{-1}) + 0.34(1\pi_u^{-2}3\pi_u) - 0.33(1\pi_u^{-1}6\sigma_u2\sigma_u^{-1})$
	$^2\Pi_u$	49.31	0.005	$0.60(2\sigma_u^{-1}5\sigma_u1\pi_u^{-1}) + 0.49(1\pi_u^{-1}5\sigma_u2\sigma_u^{-1}) - 0.43(2\sigma_u^{-1}6\sigma_u1\pi_u^{-1})$ $-0.38(1\pi_u^{-1}6\sigma_u2\sigma_u^{-1}) + 0.33(2\sigma_u^{-1}4\sigma_u1\pi_u^{-1})$ $- 0.32(2\sigma_u^{-1}2\pi_g2\sigma_g^{-1}) + 0.30(1\pi_u^{-1}4\sigma_u2\sigma_u^{-1})$
	$^2\Sigma_u^+$	49.31	0.004	
	$^2\Sigma_g^+$	49.77	0.004	$0.68(3\sigma_g^{-2}7\sigma_g) - 0.35(2\sigma_u^{-2}7\sigma_g)$
	$^2\Sigma_u^+$	49.79	0.003	$0.41(1\pi_u^{-1}3\pi_g3\sigma_g^{-1}) - 0.32(3\sigma_g^{-2}6\sigma_u)$
50.5	$^2\Sigma_u^+$	50.58	0.004	$0.48(2\sigma_g^{-1}2\pi_g1\pi_u^{-1})$
	$^2\Sigma_g^+$	51.08	0.002	$0.57(3\sigma_g^{-1}5\sigma_u2\sigma_u^{-1}) + 0.45(3\sigma_g^{-1}4\sigma_u2\sigma_u^{-1}) + 0.43(2\sigma_u^{-1}5\sigma_u3\sigma_g^{-1})$ $+ 0.41(2\sigma_u^{-1}4\sigma_u3\sigma_g^{-1}) - 0.37(2\sigma_u^{-1}6\sigma_u3\sigma_g^{-1})$
	$^2\Sigma_g^+$	51.95	0.002	$0.32(2\sigma_u^{-1}5\sigma_u3\sigma_g^{-1})$
	$^2\Sigma_u^+$	51.38	0.006	$0.35(1\pi_u^{-1}3\pi_u2\sigma_u^{-1}) + 0.35(2\sigma_u^{-2}4\sigma_u)$
	$^2\Sigma_u^+$	52.41	0.008	$0.10(2\sigma_u^{-1}) + 0.50(3\sigma_g^{-1}6\sigma_g2\sigma_u^{-1}) + 0.46(1\pi_u^{-1}3\pi_u2\sigma_u^{-1})$ $+ 0.36(2\sigma_u^{-1}6\sigma_g3\sigma_g^{-1})$
	$^2\Pi_u$	52.73	0.003	$0.76(3\sigma_g^{-1}7\sigma_g1\pi_u^{-1})$
	$^2\Sigma_g^+$	52.99	0.007	$0.44(1\pi_u^{-1}3\pi_g2\sigma_u^{-1}) + 0.38(2\sigma_u^{-1}3\pi_g1\pi_u^{-1}) - 0.32(2\sigma_u^{-1}6\sigma_u3\sigma_g^{-1})$
	$^2\Sigma_u^+$	57.87	0.004	$0.40(1\pi_u^{-1}2\pi_g2\sigma_g^{-1})$
	$^2\Sigma_u^+$	58.40	0.002	
	$^2\Sigma_g^+$	59.40	0.004	$0.43(3\sigma_g^{-1}6\sigma_u2\sigma_u^{-1})$
60	$^2\Sigma_g^+$	59.40	0.009	$0.52(3\sigma_g^{-1}6\sigma_u2\sigma_u^{-1})$
63	$^2\Sigma_g^+$	59.48	0.009	$0.45(3\sigma_g^{-1}6\sigma_u2\sigma_u^{-1})$
	$^2\Sigma_g^+$	62.70	0.003	$0.41(2\sigma_u^{-1}4\sigma_u2\sigma_g^{-1}) + 0.37(3\sigma_g^{-1}6\sigma_g2\sigma_g^{-1}) + 0.37(2\sigma_g^{-1}4\sigma_u2\sigma_u^{-1})$ $+ 0.34(2\sigma_g^{-1}6\sigma_g3\sigma_g^{-1}) - 0.30(2\sigma_u^{-1}3\sigma_u2\sigma_g^{-1})$

and intensity of the satellite states, the summed intensity of states lying closely in energy was found to be in excellent agreement with the previous calculations. We are, therefore, confident that this theoretical description can be used to discuss the behavior of states at higher binding energies above the first double-ionization threshold.

At energies above the first double-ionization threshold ($IP^{++} = 43$ eV), a broad spectral feature in the SAC-CI spectra (Fig. 4) is observed to decrease in intensity as the binding energy increases. This feature is consistent with the broad spectra observed in the present EMS binding-energy spectra and with previous XPS measurements [22]. In the higher-resolution XPS spectrum, a number of weak satellite features were observed between 40 and 50 eV, with two features at 46.3 and 48.1 eV being tentatively assigned to $^2\Pi_u$ states by consideration of the resonant Auger spectrum and empirical calculations [20]. The present SAC-CI calculation recovered three $^2\Pi_u$ states at 48.40, 48.86, and 49.31 eV

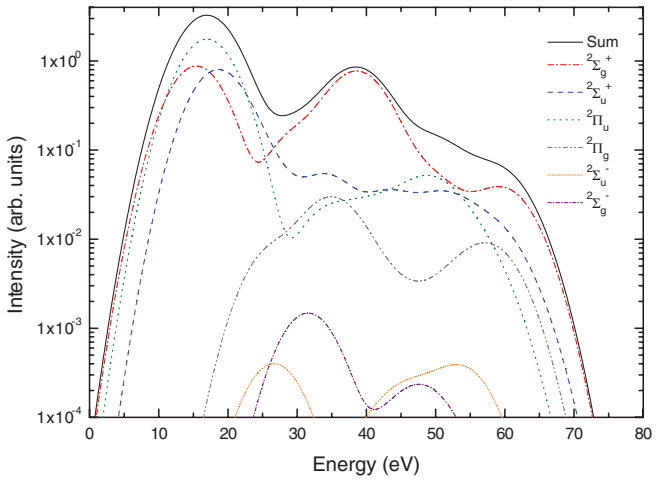

FIG. 4. (Color online) The theoretical SAC-CI binding-energy spectra, convolved with the present experimental energy resolution. Also shown are the contributions from each final-state symmetry manifold. See the text for further details.

having PSs of 0.008, 0.003, and 0.005, respectively. These states are dominated by $(2\sigma_u^{-1}1\pi_u^{-1}n\sigma_u)$ and $(1\pi_u^{-2}n\pi_u)$ configurations. The present calculation also reveals that states of $^2\Sigma_g^+$ symmetry have a considerably larger intensity in this energy region. The bulk of this intensity originates from satellites at 47.70 (PS = 0.015) and 48.19 (PS = 0.014) having dominant contributions from $(3\sigma_g^{-1}1\pi_u^{-1}n\pi_u)$ configurations. This observation is supported by previous EMS measurements where the experimental momentum profile for the binding-energy region 43.5–50 eV was tentatively assigned to $^2\Sigma_g^+$ states.

The XPS spectra also reported a broad feature at 50.5 eV. The present calculation gave three $^2\Sigma_u^+$ satellites at 50.58, 51.38, and 52.41 eV. These states had intensities of 0.004, 0.006, and 0.008 respectively. These states involved a high number of three-hole two-particle configurations that interacted with $(2\sigma_g^{-1}1\pi_u^{-1}n\pi_g)$, $(2\sigma_u^{-2}n\sigma_u)$, and $(2\sigma_u^{-1}3\sigma_g^{-1}n\sigma_g)$ configurations.

The last feature observed in the XPS spectra was a broad structure over the 58–65-eV binding-energy range. The present SAC-CI calculation suggests that this feature may arise from $^2\Sigma_g^+$ states found in this region. Specifically, two relatively intense states at 59.04 and 59.84 eV both were found to have intensities of 0.009. These states arise from significant mixing with $(2\sigma_u^{-1}3\sigma_g^{-1}n\sigma_u)$ configurations. A number of weaker $^2\Sigma_u^+$ states were also found in this region and may also contribute to the observed feature.

The prediction of many satellite states over the entire binding-energy range from the SAC-CI calculation is consistent with the results obtained from the EMS experiments with limited energy resolution. Indeed, the synthetic angle-resolved binding-energy spectra derived from the one-hole coefficients qualitatively reproduced the observed momentum dependence of the angle-resolved binding-energy spectra at higher binding energies. However, it is particularly apparent that, for binding energies above 55 eV, some of the synthetic intensity is missing when compared to the experimental spectra. This difference is attributed to a large number of weak satellite states whose one-hole configuration-interaction coefficients are not recovered in the calculation, however, one cannot entirely rule out any contribution from direct double ionization. Despite this limitation, the present calculation reveals that ionization-excitation processes are still contributing to the spectra at binding energies up to 65 eV. The spectra at binding energies above 40 eV are, therefore, partly attributed to ionization-excitation processes that produce a large number of weak $^2\Sigma_g^+$ satellites that give the s character over the entire binding-energy range and a clustering of $^2\Sigma_u^+$ and $^2\Pi_u$ satellite states that give higher angular momentum contributions.

The present paper provides a strong foundation for understanding the momentum dependence of ionization mechanisms above the first double-ionization potential. Specifically, the present results and theoretical description suggest that ionization-excitation processes make a significant partial contribution to the observed intensity under these high-energy and large momentum-transfer kinematics. Furthermore, by supplementing our experiment with a limited SAC-CI calculation, we have provided a quantitative spectral assignment to the high binding-energy features observed in the XPS spectra. Experiments with improved energy resolution would be necessary for a quantitative assessment of the individual transitions predicted by the theoretical calculation. Here, the limited energy resolution did not facilitate a direct comparison between the observed spectral intensity and the individual states' spectroscopic strengths; which would be required to assess the validity of the spectroscopic sum rules for molecules. Without the ability to directly compare spectroscopic intensities between the theoretical model and the experimental results, we cannot determine if any spectral contribution arises from a direct double-ionization process. Further experiments at different impact energies and kinematics may be required to fully characterize the ionization dynamics of these high-lying states. Such intensive experiments are becoming possible through the use of our recently developed spectrometer that offers further improvements in collection efficiency [41].

IV. CONCLUSION

The present experiments significantly expand our understanding of electron-impact ionization of states lying above the first double-ionization potential in N_2. The experiments have been supplemented with theoretical calculations that provide the first clues for understanding the mechanisms of ionization for states with high binding energies. Here, the calculations suggest that the ionization-excitation mechanisms make a significant partial contribution to the behavior at binding energies above the lowest double-ionization threshold. These calculations also provide quantitative assignments for the existing x-ray photoelectron spectrum. The classification of these features creates a pressing need for high-resolution EMS studies to clarify their role in electron-impact ionization processes. This paper represents an important step towards understanding the nature of ionization dynamics at high-impact energy and large momentum transfer where ionization-excitation processes can compete with direct double-ionization mechanisms.

ACKNOWLEDGMENTS

This research was partially supported by a Grant-in-Aid for Scientific Research (S), Grant No. 20225001 from the Japan Society for the Promotion of Science (JSPS) as well as that for JSPS Fellows, Grant No. 20-08762. D.B.J. gratefully acknowledges support from JSPS for a postdoctoral fellowship (FY2008–FY2010).

[1] I. E. McCarthy and E. Weigold, Phys. Rep. **27**, 275 (1976).
[2] I. E. McCarthy and E. Weigold, Rep. Prog. Phys. **54**, 789 (1991).
[3] M. A. Coplan, J. H. Moore, and J. P. Doering, Rev. Mod. Phys. **66**, 985 (1994).
[4] E. Weigold and I. E. McCarthy, *Electron Momentum Spectroscopy* (Kluwer Academic/Plenum, New York, 1999).
[5] V. G. Neudatchin, Y. V. Popov, and Y. F. Smirnov, Phys. Usp. **42**, 1017 (1999).
[6] M. Takahashi, Bull. Chem. Soc. Jpn. **82**, 751 (2009).
[7] M. Takahashi, N. Watanabe, Y. Khajuria, K. Nakayama, Y. Udagawa, and J. H. D. Eland, J. Electron Spectrosc. Relat. Phenom. **141**, 83 (2004).
[8] M. Takahashi, N. Watanabe, Y. Khajuria, Y. Udagawa, and J. H. D. Eland, Phys. Rev. Lett. **94**, 213202 (2005).
[9] D. B. Jones, M. Yamazaki, N. Watanabe, and M. Takahashi (unpublished).
[10] W. Eberhardt, E. W. Plummer, I.-W. Lyo, R. Carr, and W. K. Ford, Phys. Rev. Lett. **58**, 207 (1987).
[11] J. Berakdar, A. Lahmam-Bennani, and C. Dal Cappello, Phys. Rep. **374**, 91 (2003).
[12] D. B. Jones, M. Yamazaki, N. Watanabe, and M. Takahashi, Phys. Rev. A **83**, 012704 (2011).
[13] M. Takahashi, Y. Miyake, N. Watanabe, Y. Udagawa, Y. Sakai, and T. Mukoyama, Phys. Rev. Lett. **98**, 013201 (2007).
[14] P. Baltzer, M. Larsson, L. Karlsson, B. Wannberg, and M. Carlsson Gothe, Phys. Rev. A **46**, 5545 (1992).
[15] T. Aoto, K. Ito, Y. Hikosaka, A. Shibasaki, R. Hirayama, N. Yamamono, and E. Miyoshi, J. Chem. Phys. **124**, 234306 (2006).
[16] J. P. D. Cook, R. Pascual, E. Weigold, W. Von Niessen, and P. Tomasello, Chem. Phys. **141**, 211 (1990).
[17] S.-F. Zhang, C.-G. Ning, Y.-R. Huang, K. Lui, and J. K. Deng, Acta Phys. Sin. **58**, 2382 (2009).
[18] M. Ehara, M. Ishida, and H. Nakatsuji, Collect. Czech. Chem. Commun. **70**, 881 (2005).
[19] Y. R. Miao, C. G. Ning, and J. K. Deng, Phys. Rev. A **83**, 062706 (2011).
[20] W. Eberhardt, E. W. Plummer, I.-W. Lyo, R. Murphy, R. Carr, and W. K. Ford, J. Phys., Colloq. **48**, C9-679 (1987).
[21] W. E. Moddeman, T. A. Carlson, M. O. Krause, B. P. Pullen, W. E. Bull, and G. K. Schweitzer, J. Chem. Phys. **55**, 2317 (1971).
[22] S. Svensson, M. Carlsson-Gothe, L. Karlsson, A. Nilsson, N. Martensson, and U. Gelius, Phys. Scr. **44**, 184 (1991).
[23] W. F. Ford, Phys. Rev. **133**, B1616 (1964).
[24] W. Kohn and L. J. Sham, Phys. Rev. **140**, A1133 (1965).
[25] P. Duffy, D. P. Chong, M. E. Casida, and D. R. Salahub, Phys. Rev. A **50**, 4707 (1994).
[26] M. E. Casida, Phys. Rev. A **51**, 2005 (1995).
[27] P. Duffy, Can. J. Phys. **74**, 763 (1996).
[28] H. Nakatsuji, Chem. Phys. Lett. **177**, 331 (1991).
[29] M. Ehara and H. Nakatsuji, Chem. Phys. Lett. **282**, 347 (1998).
[30] Q. G. Tian, J. Yang, Y. F. Shi, X. Shan, and X. J. Chen, J. Chem. Phys. **136**, 094306 (2012).
[31] T. H. Dunning, Jr., J. Chem. Phys. **53**, 2823 (1970). Basis set obtained from the Basis Set Exchange Vol. 1.2.2, Environmental Molecular Sciences Laboratory Basis Set Library, U.S. Department of Energy, Pacific Northwest Laboratory.
[32] T. H. Dunning, Jr. and P. J. Hay, in *Methods of Electronic Structure Theory*, edited by H. F. Schaefer III (Plenum, New York, 1977), Vol. 3. Basis set obtained from the Basis Set Exchange Vol. 1.2.2, Environmental Molecular Sciences Laboratory Basis Set Library, U.S. Department of Energy, Pacific Northwest Laboratory.
[33] A. D. Becke, J. Chem. Phys. **98**, 5648 (1993).
[34] C. Lee, W. Yang, and R. G. Parr, Phys. Rev. B **37**, 785 (1988).
[35] T. H. Dunning, Jr., J. Chem. Phys. **90**, 1007 (1989).
[36] R. A. Kendall, T. H. Dunning, Jr., and R. J. Harrison, J. Chem. Phys. **96**, 6796 (1992).
[37] A. O. Bawagan, C. E. Brion, E. R. Davidson, and D. Feller, Chem. Phys. **113**, 19 (1987).
[38] J. N. Migdall, M. A. Coplan, D. S. Hench, J. H. Moore, J. A. Tossell, V. H. Smith, Jr., and J. W. Liu, Chem. Phys. **57**, 141 (1981).
[39] M. J. Frisch *et al.*, GAUSSIAN 98, Revision A.7, Gaussian, Inc., Pittsburgh, PA, 1998.
[40] M. J. Frisch *et al.*, GAUSSIAN 03, Revision B.05, Gaussian Inc., Pittsburgh, PA, 2003.
[41] M. Yamazaki, H. Satoh, M. Ueda, D. B. Jones, Y. Asano, N. Watanabe, A. Czasch, O. Jagutzki, and M. Takahashi, Meas. Sci. Technol. **22**, 075602 (2011).